PHYSICAL REVIEW FLUIDS **4**, 123601 (2019)

Bretherton's buoyant bubble

Wassim Dhaouadi[1,2] and John M. Kolinski[1]
[1]*École Polytechnique Fédérale de Lausanne, 1015 Lausanne, Switzerland*
[2]*ETH Zürich, 8093 Zürich, Switzerland*

(Received 11 February 2019; published 2 December 2019)

When a buoyant bubble is inserted into a closed capillary that is slightly smaller than the capillary length, it appears stuck; exactly why this is so is a puzzle that has remained unanswered over the past 50 years. Recent calculations suggest that the bubble's motion is critically dependent on the hydrodynamics of the surrounding liquid film; however, quantitative measurements of these dynamics are lacking. We provide direct measurements of the dynamics of the liquid film surrounding a "stuck" bubble, recorded using interference microscopy. The film slowly relaxes to a constant thickness, and is stabilized by disjoining pressure at long times. The film's stability at this thickness is demonstrated by recovery after applied thermal perturbations; thus, we confirm that Bretherton's buoyant bubble is not pinned at a contact line, but is instead ostensibly stuck by extraordinarily slow flow in the surrounding liquid film whose thickness is set by a balance of capillary stress and disjoining pressure.

DOI: 10.1103/PhysRevFluids.4.123601

I. INTRODUCTION

Confinement of gas within a liquid-filled channel arises in myriad natural and technological processes, from carbon sequestration [1–4] and hydrocarbon recovery [5,6] to circulatory systems in biology [7–11]. Indeed, modern microfluidic applications [12–14] often involve several phases of fluid. Gas confined in liquid filled channels often forms a bubble, whose motion and dynamics depend on the boundary conditions, physical dimensions of the flow, and the thermodynamic state of the fluid [15–18]. Over a century ago it was observed that bubbles in a sealed vertical channel with a sufficiently narrow diameter cease to rise, and appear stuck [17]. Analysis of the flow around such confined bubbles showed that under a certain critical confinement, there is no bubble shape solution that allows it to rise, thus drastically altering the flow dynamics from the basic lubrication assumption. While a bubble that remains stuck in a solid is unsurprising because the solid resists shear deformation, a Newtonian fluid cannot provide any resistance at zero velocity, and we expect that the bubble will rise due to buoyancy. Indeed, our intuition tells us that an immiscible phase will always rise in a denser one, demanding that we reconcile intuition with long-standing observations. A recent theoretical analysis of this liquid film uses asymptotic matching to predict a self-similar pinch-off singularity of the thin film surrounding the bubble that prevents any flow and ultimately stops the bubble [19]; however, experimental measurements of the dynamics of this film are lacking, and the physical mechanisms governing the dynamics of the bubble in this important limit remain unclear.

In this paper, we measure the dynamics of the thin film surrounding buoyant bubbles confined within thin glass capillary tubes that are sealed on one end. Through our measurements we identify a length scale, at which the film will stabilize and cease to drain, suggesting another avenue for the theoretical treatment of the problem. All experiments take place under completely wetting conditions: Isopropanol (IPA) is used as the fluid and as a nonpolar solvent wets the glass with a negligible contact angle, averting contact line pinning. Bubbles confined within capillaries of different radii enable us to probe the effect of capillary size on the film dynamics.

The bubble appears stuck when the channel diameter is comparable to the liquid capillary length $\ell_c = \sqrt{\frac{\gamma}{\rho g}}$ [20]. For round capillaries of radius R, the critical capillary radius is calculated to be $R_{\mathrm{cr}} = 0.918\ell_c$ [21]. Below this critical size, the effects of surface tension and gravity are of the same order; the relative importance of these effects is evaluated using the dimensionless Bond number, given in terms of the capillary length by $\mathrm{Bo} = (\frac{R}{\ell_c})^2$; thus the critical bond number is $\mathrm{Bo}_{\mathrm{cr}} = 0.842$. A recent asymptotic analysis of the thin film bounding the gas bubble for $R < R_{\mathrm{cr}}$ predicts that the liquid film surrounding the bubble will drain to zero thickness in infinite time [19]. For films draining due to gravity, the ever-decreasing thickness provides a means by which viscous resistance in the film will increase [22]; however, the calculated film dynamics are nonlinear. While similar experiments have been carried out recently [22,23], important aspects of the confinement of the bubble are due to a uniform bounding film, where the bubble is conformal to the container.

II. EXPERIMENTAL METHODS

The liquid surrounding the gas is imaged at the wall of the capillary using a low coherence length Fizeau interferometry microscope. The film is illuminated with a collimated light-emitting diode (LED) that is focused on the capillary's inner surface with a microscope objective, as shown in Fig. 1(a). A beam splitter directs the light source onto the imaging path. A high-sensitivity CCD camera records the interference signal in a manner similar to that used to study high velocity droplet impacts [24], although in this case the phase of the second reflection is not shifted by π on account of the adjacency of the liquid and glass layers. The microscope objective's narrow depth of field [25], and the LED's low coherence length [26] ensure that interference fringes appear only in the focus area, and only upon reflection from the glass-liquid and liquid-air interfaces. Reflections on other interfaces along the imaging path do not affect the signal.

A typical image of a bubble stuck within a capillary is shown in Fig. 1(b). The region of interest corresponds to a narrow band at the center of the capillary [27]. Bubbles are formed by injecting air into the capillary using a syringe with a long and narrow tip. Bubble size is controlled to ensure the generation of an elongated Bretherton bubble such that $\alpha = \frac{R_{\mathrm{eq}}}{R} > 1$, where R_{eq} is the radius of a perfectly spherical bubble with an equivalent volume of gas. Over a period of 1 or 2 days, no motion of the bubble can be detected and the bubble appears to be stuck.

The region of interest captures the film and transition region connecting the film to both the top and the bottom menisci as shown in Fig. 1(c). The modulations in the observed intensity field appear due to interference between light reflected from the glass-IPA interface and from the IPA-saturated air interface, and can be used to determine the film's thickness according to the expression [28]

$$h(x, y) = \frac{\lfloor \frac{k+1}{2} \rfloor \lambda}{2n} + (-1)^k \frac{\lambda}{2\pi n} \arccos \sqrt{\frac{I - I_{\mathrm{min}}}{I_{\mathrm{max}} - I_{\mathrm{min}}}}, \tag{1}$$

where $n = 1.38$ is the refractive index of IPA, k the fringe order, λ the wavelength of the light source, and I_{min} and I_{max} are the local intensities of the troughs and peaks, respectively, effectively correcting for illumination inhomogeneity. The intensity mapping to height varies with the phase of the interference pattern. Absolute height is measured by tracking the spatiotemporal evolution of the film from the dewetted state of the film with zero thickness obtained through thermal perturbation as described below.

III. RESULTS

We consistently observe a thin liquid film surrounding the bubble at steady state for Bond numbers below the critical Bo identified by Bretherton. For $\mathrm{Bo} = 0.082$, we measure a film thickness of approximately 40 nm after waiting several days [Fig. 1(c)]. The presence of the film

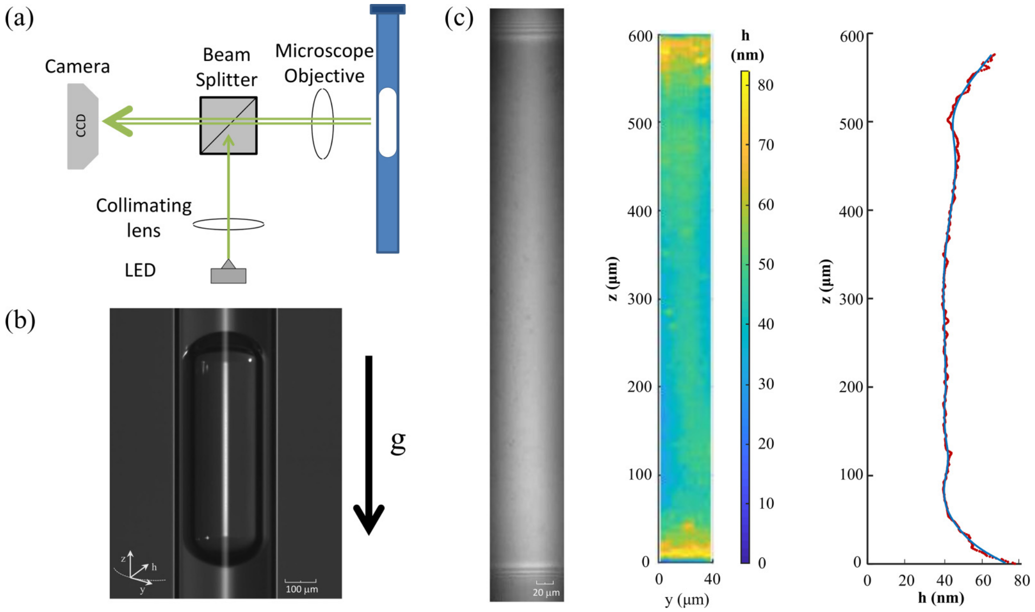

FIG. 1. Visualizing the thin film around the bubble with Fizeau interferometry. (a) Schematic of the experimental setup: A collimated LED source is focused onto the capillary's internal surface by a microscope objective. Reflection from the glass-liquid interface interferes with the reflection from the liquid-air interface, forming an interference pattern. (b) Typical image of Bretherton's buoyant bubble in a sealed capillary, $2R = 0.33$ mm (Bo $= 0.009$). The bubble appears stationary over a timescale of days. (c) Interferogram of a section of the film around the bubble recorded several hours after its formation; here, $2R = 1$ mm (Bo $= 0.082$). The intensity profile is converted to the film thickness as described in the main text. Thickness is averaged over the y coordinate, yielding the bubble profile shown at right; raw data (red) are smoothed in z using local averaging to show the shape of the bubble (blue). Averaging in this manner controls for imaging noise and submicron dirt on the capillary's surface.

demonstrates that the bubble shape that eluded Bretherton in his initial calculations [21] indeed initially exists. We also note a smooth transition, visible for approximately 50 μm in the image, connecting the flat film to the menisci. The transition region extends beyond the depth of field of our interferometric imaging modality, and thus we cannot place firm constraints on its extent.

Given that the bubble is not stuck by contact line pinning, it can still rise—at what velocity might we expect the bubble to ascend? We can calculate the rise velocity due to displacement of the fluid by gravitational drainage through the nanometer-scale film using the lubrication approximation [29]. The rise velocity of the bubble is calculated to be $U = \frac{2\rho g h^3}{3\mu R}$ or 1.6×10^{-13} m/s (i.e., 14 nm per day). Lateral resolution of the imaging system is limited to 1 μm per pixel by diffraction; thus the bubble rises by approximately 1% of a pixel per day, well below our resolution.

For a typical bubble, the buoyant force is proportional to the displaced volume; thus we probe the role of buoyancy by changing the gas volume within the bubble. To this end, different sized bubbles were introduced into sealed capillaries and allowed to reach a steady state under the same ambient conditions, (inset of Fig. 2). The mean film height and its standard deviation are shown for bubbles of different sizes in Fig. 2. The graph shows a typical value of 2 nm variance along each bubble length, confirming that for a fixed Bo, not only is the film extremely flat, but the bubble volume along the region where the film is flat, away from the caps, does not affect the film thickness. The observed independence of the bubble's state from the bubble size is consistent with the earliest observations of confined bubbles rising in capillaries over the critical condition [17,30]; we observe that this

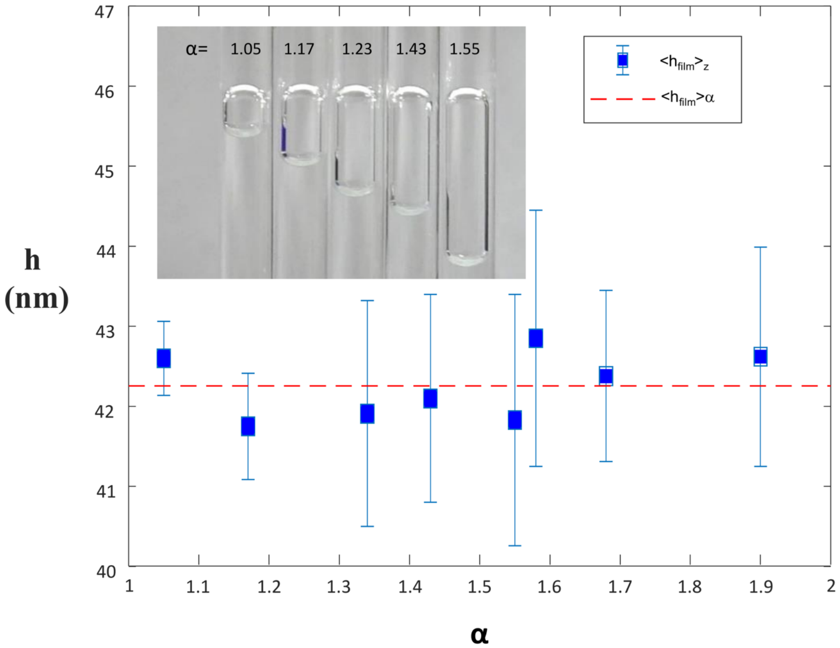

FIG. 2. Different gas volume bubbles at steady state. Bubbles with increasing volumes of gas were inserted into capillaries with $\mathrm{Bo} = 0.123$. The ratio of the radius of the equivalent-volume spherical bubble to the capillary radius α is shown with five example bubbles (inset). A waiting period of 48 h transpired before the average value of the steady-state film thickness was measured over the region of the liquid film between the bubble menisci $\langle h_{\mathrm{film}}\rangle_z$. The steady-state heights are identical within the measured variability in z, as can be seen by the average value of these data points for all values of α, $\langle h_{\mathrm{film}}\rangle_\alpha$, represented by the dashed red line.

phenomenon extends to bubbles under the critical condition. Moreover, the flatness of the film for $R < R_{\mathrm{cr}}$ contrasts with the observation of ripples at the lower part of moving bubbles [17,31,32]. Such ripples are due to hydrodynamic stresses and strongly depend on the capillary number Ca, which vanishes for the quasistatic rise.

To investigate the stability of the observed film, we employ a protocol of thermal perturbations to deliberately drive the surrounding film out of equilibrium and study the dynamics of its recovery. After the initial formation of the bubble, we wait a few days until no variations in the film profile are observed, and the film is flat to within our experimental resolution. We first observe a steady-state uniform flat film of thickness 85 nm as shown in Fig. 3(c). At this time, we briefly apply a heat probe to the side of the capillary closest to the camera; this excites thermal-Marangoni stresses in the thin film, causing it to dewet from the side of the capillary nearest the camera in a first timescale $\tau_1 \sim 1$ s. The film dewetted in this manner is used as a reference state to obtain absolute film thickness measurements with the interferometric microscope. Because the heat application is brief, only the film is heated, and the bubble remains at ambient temperature; thus, we can reasonably suppose that the gas dilation and change of viscosity upon this heat perturbation is negligible. The heat from the probe causes the temperature of the film to locally increase, and its surface tension to locally decrease, inducing an azimuthal flow; the velocity of the dewetting process matches the calculated velocity V for thermally excited Marangoni stresses as estimated from the surface tension gradient $\frac{d\gamma}{dx}$ induced by the temperature gradient $\frac{dT}{dx}$ [33,34],

$$V = \frac{h\tau}{2\mu}, \quad \text{with} \quad \tau = \frac{d\gamma}{dx} = \frac{d\gamma}{dT}\frac{dT}{dx}. \tag{2}$$

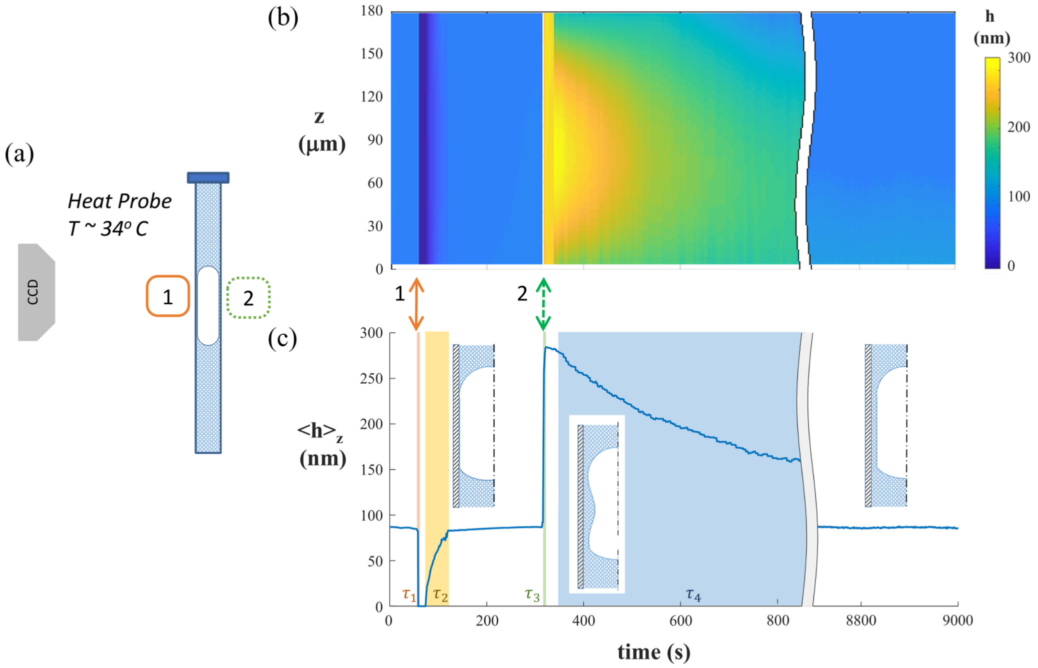

FIG. 3. Thermocapillary perturbations to the film in a $2R = 2$ mm (Bo = 0.329) capillary show four distinct timescales. (a) A thermal perturbation at 34 °C is applied in succession to opposite sides of the capillary, which is held at an ambient temperature of 23 °C. A heat probe is applied first to the side nearest the camera for a fraction of a second (1), and then removed while the film recovers; the heat probe is then applied to the side of the capillary opposite from the camera for a second (2), and then removed. (b) Film profile evolution in response to the thermal perturbation with a temporal resolution of 1 s. The mean of the height in z, shown below the height map, reveals persistent recovery to a constant thickness from both perturbations, suggesting that the film attains a finite thickness at steady state. The schematic representations of the bubble illustrate the film profile during the experiment. The gray curved lines indicate time elapsed after the second step of the perturbation protocol.

For IPA, $\frac{d\gamma}{dx} = -30 \times 10^{-5}$ N/mK, In our case, a 5 °C perturbation results in $\frac{dT}{dx} \sim 10^3$ K/s with $h \sim 10^{-7}$ m and assuming $\mu = 2 \times 10^{-3}$ Pa/s gives $V \sim 1$ mm/s, consistent with the observed dewetting timescale. As this dewetting occurs, a contact line forms at the extremity of the menisci at the interface. However, this state is not stable. The zero thickness and contact lines do not persist, and the film recovers back to its previous state after a second timescale $\tau_2 \sim 1$ min, as shown by the height plot in Fig. 3(c).

After τ_2 elapses, a similar perturbation is applied to the side of the capillary opposite from the camera, causing the observed portion of the film to become thicker within $\tau_3 \sim 1$ s; τ_3 is also due to thermally excited Marangoni stresses. Applying the heat probe to the opposite side of the capillary causes the film closest to the camera to burgeon in thickness, with the z-averaged height $\langle h \rangle_z$ approaching 300 nm. As the film thickens, we observe the formation of a dimple in the middle of the bubble, slightly skewed toward the bottom. Over a timescale $\tau_4 \sim 6000$ s, the film resumes the same steady-state thickness as it had when we applied the first perturbation. A space-time graph of the film's thickness in response to the applied perturbations is shown in Fig. 3(b), strongly indicating the stability of the observed film thickness. Such perturbations show that the zero-thickness film is not an energetically favored state of the bubble, rather a very thin film of uniform thickness is robust to perturbations.

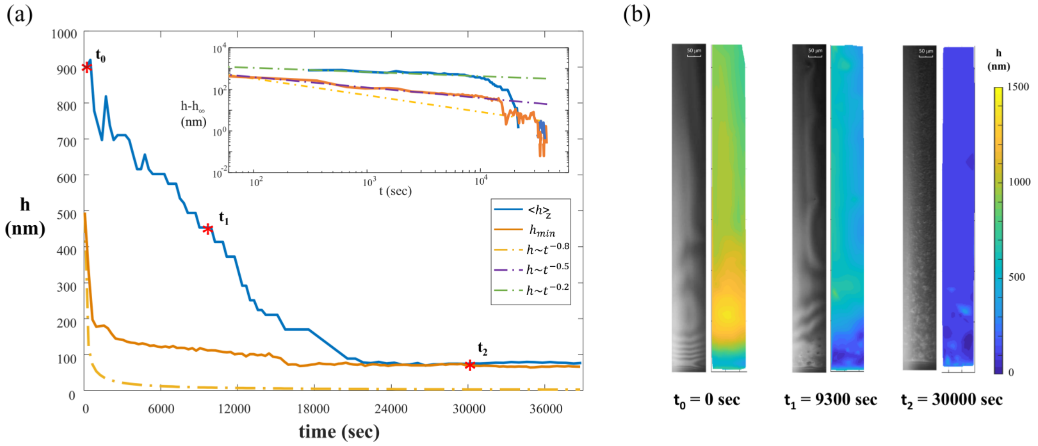

FIG. 4. Initial drainage dynamics immediately after formation of the bubble in a capillary with $2R = 1.58$ mm ($\mathrm{Bo} = 0.205$). The minimum height corresponding to the bottom meniscus transition region (orange) and the mean height (blue) are plotted as a function of time after the bubble is inserted into the capillary. Initially the film is nonuniform, and not cylindrically symmetric, with a gravity biased dimple as can be seen in the interferogram and corresponding height map in (b) for t_0. Over 2 h later, the dimple has drained on average, and the film has become flatter, as can be seen by the interferogram and the height map shown at t_1. The film breaks azimuthal symmetry, perhaps due to residual submicron scale dirt on the glass surface remaining after the meticulous cleaning protocol. After over 8 h have elapsed, the film has reached an apparent steady state at a symmetric, uniform thickness of approximately 70 nm as shown in (b) at t_2. The drainage dynamics are shown on a log-log scale (inset), suggesting that $h_{\mathrm{min}} \sim t^{-0.5}$; this scaling may be self-similar, as shown by the collapse of the h-x profiles, as shown in the Supplemental Material [35]. The calculated drainage scaling for a 2D bubble $h_{\mathrm{min}} \sim t^{-\frac{4}{5}}$ [19] using the experimentally observed initial value (gold) is shown for comparison. A scaling of film thickness to the power 1/2 is expected at the *base* of the bubble, however [19].

Throughout the series of perturbations, the top meniscus is observed to be stationary. Provided that the top of the capillary is sealed, the excess fluid in the film's dimple must drain towards the bottom of the bubble, seemingly driven by a gravitational body force. We note that during this drainage the film pinches down locally in the meniscus-film transition region. The minimal thickness converges to a nonzero thickness in ∼30 000 s. This pinching corresponds to the relaxation of the menisci towards its steady-state shape with gravity and capillary stresses in balance. All excess fluid in the dimple drains through this nanometer-scale neck, which limits the overall drainage rate. The mean height of the film takes roughly ten times longer to reach equilibrium during τ_4. Assuming pure gravitational drainage through the pinch-off region, the volumetric flux per unit length along the circumference is calculated by a Poiseuille flow between a wall and a free surface to be $Q = \frac{\rho g h^3}{3\mu}$, hence the decrease in mean film thickness Δh over a time Δt can be estimated to be $\frac{\Delta h}{\Delta t} \sim \frac{Q}{h}$, corresponding to a rate of 0.16 nm/s for a bubble size similar to the one presented in Fig. 4. We observe a mean drainage rate of $\frac{\Delta \langle h \rangle_z}{\Delta t} = 0.05$ nm/s, which is comparable to the aforementioned prediction from gravitational drainage, as shown in Fig. 4. The discrepancy may be due to the low-frequency thermally induced fluctuations visible in the film that can temporarily thicken, effectively slowing the drainage. The drainage dynamics confirm that flows develop even at such small scales, suggesting that the bubble can still rise at the extraordinarily slow velocity calculated above.

The relaxation dynamics is of particular physical significance as it is an essential characteristic of the system [19]. It can be extracted from the temporal response of the film, which allows a direct comparison with theoretical calculations developed for the two-dimensional (2D) case. After bubble insertion, the temporal response of the film with $\mathrm{Bo} = 0.197$ allows us to compare our experimental results with theoretical calculations in 2D [19]. The film drains nonmonotonically

TABLE I. Measured film thickness values h_{measured}, for capillaries of various inner diameters $2R$, are tabulated with Bo, the predicted thickness $h_{\text{predicted}}$ based on the estimation provided in the Appendix, and the Hamaker constant for a glass-IPA-air system obtained from Ref. [37]. Discrepancies between measured values and predicted values might arise due to other interfacial effects such as electrostatic or retarded van der Waals forces [37,38]. The corresponding figure reference is provided in the first column.

Figure	$2R$ (mm)	Bo	$h_{\text{predicted}}$ (nm)	h_{measured} (nm)
1	1.00	0.082	40.6	41
2	1.22	0.123	43.3	42
3	2.00	0.329	58.6	85
4	1.58	0.205	49.9	68

towards a steady-state value of approximately 70 nm as shown in Fig. 4. Low-frequency fluctuations are observed on the film when the film is thicker than 200 nm, and may explain discrepancies in the observed drainage rate from the purely gravitational prediction. Such ripples are absent from a purely hydrodynamic framework. These fluctuations seem to be correlated to temperature fluctuations (not shown) that we measured to be in the order of 0.1 K in the surrounding environment of the capillary.

The film's thickness takes on a minimal value $h_{\min}$ in the region adjacent to the bottom meniscus. The bubble reaches its steady state as this thickness slowly reduces; this can be seen for a freshly inserted bubble in Fig. 4(a), and the corresponding profiles shown in Fig. 4(b). $h_{\min}$ converges to a nonzero steady value in finite time following an apparent intermediate scaling of $t^{-0.5}$, as can be seen in the inset to Fig. 4(a). This convergence rate is slower that the theoretical prediction for the 2D case [19]; extensions of this theoretical prediction to 3D including the effect of disjoining pressure are under development [36]. It can be seen from the main graph that $h_{\min}$ does not converge to zero.

Our experiments show that in contrast to theoretical predictions for a bubble in a closed capillary below a critical size [21], a thin film persists in wetting the glass surface at a steady-state thickness h_∞, whose specific value depends on the capillary's radius in a manner consistent with stabilization due to disjoining pressure, as shown in Table I. The values are compared to those obtained theoretically by balancing the disjoining and capillary pressures; this calculation is developed in detail in the Supplemental Material [35]. We also note from our analysis the emergence of a factor accounting for the additional capillary pressure due to the unmatched curvature of the end of the caps, which, together with the Laplace pressure jump at the lateral film $\frac{\gamma}{R}$, is balanced by the disjoining pressure. Results tabulated for several different capillary diameters show good agreement with this calculation, as can be seen in Table I. This is consistent with Bretherton's claim that the film thickness is uniquely determined by the conditions on the leading edge of the bubble [21].

IV. DISCUSSION

The observed film suggests a regularization mechanism for the predicted singularity in the film's drainage, and significantly alters the drainage dynamics in comparison with an existing analysis. Interestingly, a recent analysis of driven bubbles influenced by disjoining pressure of a *nonwetting* fluid shows the importance of disjoining pressure in *destabilizing* the film surrounding the bubble [18], suggesting that the dynamics we observe would be drastically altered for a nonwetting fluid.

Our observations suggest that the approach to h_∞ might be self-similar, as $h_{\min} - h_\infty$ appears to scale as $t^{-0.5}$. We show that the height profiles will indeed collapse when rescaled by this exponent of t in the Supplemental Material [35]. While these dynamics are different than the $h_{\min}$ scaling calculated for the 2D geometry, they are consistent with the temporal scaling at the bottom of the bubble, suggesting that this asymptotic analysis could be accurate until the disjoining pressure becomes large [19]; furthermore, our experiments are necessarily fully 3D, which could alter the scaling of the film thickness in time.

In order to probe the stability of h_∞, we perturbed the film with a thermal probe, inducing Marangoni stresses due to a gradient in surface tension. An estimation of the surface tension gradient generated this way is used to develop a prediction for the timescale observed in the flow of the film as described above; this flow is predicted to occur over seconds, consistent with our observations of τ_1 and τ_3. Phenomenology related to thermal excitation in this problem could be interesting to explore in future work, as we have shown that Marangoni stresses arising from temperature gradients can significantly alter the film's state, and thus small fluctuations of temperature play a dominant role in the dynamics; this can be seen directly from the unsteady nature of the film drainage shown in Fig. 4. We note that our experiments show the liquid film dewetting to zero thickness in response to Marangoni stresses, suggesting that there is a nonperturbative limit where the film's stability in response to thermal excitation is not unconditionally stable for all wave numbers. This would be interesting to see in a complete theoretical development, as these dynamics might be rich.

Irrespective of bubble size, we find that the film surrounding the bubble is extremely flat, implying that the pressure along the film is constant. As opposed to unconfined bubbles in liquids, where the pressure gradient along the gas-liquid interface is hydrostatic, and buoyancy corresponds to the total volume of displaced fluid, the thin film breaks the continuity of the hydrostatic pressure gradient [35]. Gravity becomes a body force driving flow in the film and the buoyancy force of such a bubble corresponds to a reduced volume of the displaced fluid. Here, $-\vec{F}_{\text{buoyancy}} = \iint_S \vec{\nabla} P \cdot d\vec{n} = \iint_{S_{\text{caps}}} \vec{\nabla} P \cdot d\vec{n} = \iiint_{V_{\text{caps}}} \rho \vec{g} dV$, where S_{caps} and V_{caps} refer to the surface area and volume of the bubbles caps, or the menisci, at the ends of the bubble. Thus a bubble under such confinement has a complex surface stress condition, resulting in its nonintuitive behavior.

Upon varying the bubble size relative to the capillary diameter, we encounter a potentially interesting limit not directly discussed or considered in the calculations of this problem, where α approaches 1; in this case, the volume of gas contained in the bubble is insufficient to push against the wall of the capillary, and generate a thin boundary film. Instead in this case the bubble will rise, even when $R < R_c$. We observed a significant unsteadiness of the velocity for bubbles near this limit in yet another apparently critical scenario for confined bubbles that merits further investigation in order to gain insight into the precise role of van der Waals stresses in causing the counterintuitive effective arrest of Bretherton's buoyant bubble.

ACKNOWLEDGMENTS

We gratefully acknowledge helpful comments from François Gallaire, Ludovic Kaiser, Töbias Schneider, Jens Eggers, and Howard Stone. Project supported by EMSI startup funds at EPFL.

---

[1] M. Y. Corapcioglu, A. Cihan, and M. Drazenovic, Rise velocity of an air bubble in porous media: Theoretical studies, Water Resour. Res. **40**, W04214 (2004).

[2] S. Wang and A. F. Clarens, The effects of CO_2-brine rheology on leakage processes in geologic carbon sequestration, Water Resour. Res. **48**, (2012).

[3] C. M. Oldenburg and J. L. Lewicki, On leakage and seepage of CO_2 from geologic storage sites into surface water, Environ. Geol. **50**, 691 (2006).

[4] S. Wang, I. M. Edwards, and A. F. Clarens, Wettability phenomena at the CO_2–brine–mineral interface: Implications for geologic carbon sequestration, Environ. Sci. Technol. **47**, 234 (2012).

[5] C. M. Oldenburg, K. Pruess, and S. M. Benson, Process modeling of CO_2 injection into natural gas reservoirs for carbon sequestration and enhanced gas recovery, Energy Fuels **15**, 293 (2001).

[6] K. Blok, R. H. Williams, R. E. Katofsky, and C. A. Hendriks, Hydrogen production from natural gas, sequestration of recovered CO_2 in depleted gas wells and enhanced natural gas recovery, Energy **22**, 161 (1997).

[7] A. Vilagrosa, E. Chirino, J.-J. Peguero-Pina, T. S. Barigah, H. Cochard, and E. Gil-Pelegrin, *Plant Responses to Drought Stress* (Springer, Berlin, 2012).

[8] J. Ryu, B. G. Hwang, and S. Lee, *In vivo* dynamic analysis of water refilling in embolized xylem vessels of intact *Zea mays* leaves, Ann. Bot. **118**, 1033 (2016).

[9] C. R. Brodersen, A. J. McElrone, B. Choat, M. A. Matthews, and K. A. Shackel, The dynamics of embolism repair in xylem: *In vivo* visualizations using high-resolution computed tomography, Plant Physiol. **154**, 1088 (2010).

[10] P. Preira, M. P. Valignat, J. Bico, and O. Théodoly, Single cell rheometry with a microfluidic constriction: Quantitative control of friction and fluid leaks between cell and channel walls, Biomicrofluidics **7**, 24111 (2013).

[11] D. S. Hariprasad and T. W. Secomb, Motion of red blood cells near microvessel walls: Effects of a porous wall layer, J. Fluid Mech. **705**, 195 (2012).

[12] P. Hadikhani, S. M. H. Hashemi, G. Balestra, L. Zhu, M. A. Modestino, F. Gallaire, and D. Psaltis, Inertial manipulation of bubbles in rectangular microfluidic channels, Lab Chip **18**, 1035 (2018).

[13] L. Mazutis, J. Gilbert, W. L. Ung, D. A. Weitz, A. D. Griffiths, and J. A. Heyman, Single-cell analysis and sorting using droplet-based microfluidics, Nat. Protoc. **8**, 870 (2013).

[14] C. N. Baroud, F. Gallaire, and R. Dangla, Dynamics of microfluidic droplets, Lab Chip **10**, 2032 (2010).

[15] G. Balestra, L. Zhu, and F. Gallaire, Viscous Taylor droplets in axisymmetric and planar tubes: From Bretherton's theory to empirical models, Microfluid. Nanofluid. **22**, 67 (2018).

[16] G. Gallino, L. Zhu, and F. Gallaire, The stability of a rising droplet: An inertialess non-modal growth mechanism, J. Fluid Mech. **786**, R2 (2016).

[17] A. H. Gibson, On the motion of long air-bubbles in a vertical tube, London, Edinburgh Dublin Philos. Mag. J. Sci. **26**, 952 (1913).

[18] N. H. Hammoud, P. H. Trinh, P. D. Howell, and H. A. Stone, Influence of van der Waals forces on a bubble moving in a tube, Phys. Rev. Fluids **2**, 063601 (2017).

[19] C. Lamstaes and J. Eggers, Arrested bubble rise in a narrow tube, J. Stat. Phys. **167**, 656 (2017).

[20] IPA has a capillary length of $\ell_c = 1.743$ mm at 23 °C note that this length is sensitive to the temperature.

[21] F. P. Bretherton, The motion of long bubbles in tubes, J. Fluid Mech. **10**, 166 (1961).

[22] J. Bico and D. Quéré, Rise of liquids and bubbles in angular capillary tubes, J. Colloid Interface Sci. **247**, 162 (2002).

[23] A. Huerre, O. Theodoly, A. M. Leshansky, M.-P. Valignat, I. Cantat, and M.-C. Jullien, Droplets in Microchannels: Dynamical Properties of the Lubrication Film, Phys. Rev. Lett. **115**, 064501 (2015).

[24] M. M. Driscoll and S. R. Nagel, Ultrafast Interference Imaging of Air in Splashing Dynamics, Phys. Rev. Lett. **107**, 154502 (2011).

[25] Mitutoyo Plan Apo long working distance objective: depth of field DOF $= \pm 14\,\mu$m, magnification $= 5\times$, numerical aperture N.A. $= 0.14$, focal length $f = 40$ mm.

[26] $l_{\text{coh}} = \frac{l_{\text{FWHM}}}{2} = 3.1\,\mu$m.

[27] This is the only region in focus due to the curvature of the capillary and the narrow depth of field of the optical setup.

[28] E. Hecht and A. Zajac, *Optics* (Addison-Wesley, Reading, MA, 1974), Vol. 19872, p. 350.

[29] Boundary conditions are conventional: no slip at the solid wall, no tangential stresses at the liquid/gas interface.

[30] G. Barr, The air-bubble viscometer, London, Edinburgh Dublin Philos. Mag. J. Sci. **1**, 395 (1926).

[31] J. Ratulowski and H.-C. Chang, Transport of gas bubbles in capillaries, Phys. Fluids A **1**, 1642 (1989).

[32] H. L. Goldsmith and S. G. Mason, The movement of single large bubbles in closed vertical tubes, J. Fluid Mech. **14**, 42 (1962).

[33] X. Fanton, A. M. Cazabat, and D. Quéré, Thickness and shape of films driven by a Marangoni flow, Langmuir **12**, 5875 (1996).

[34] A. M. Cazabat, F. Heslot, S. M. Troian, and P. Carles, Fingering instability of thin spreading films driven by temperature gradients, Nature (London) **346**, 824 (1990).

[35] See Supplemental Material at http://link.aps.org/supplemental/10.1103/PhysRevFluids.4.123601 for supplemental figures and analysis.

[36] J. Eggers and H. Stone (private communication).

[37] J. Israelachvili, *Intermolecular and Surface Forces* (Academic, London, 1992).

[38] G. F. Teletzke, H. T. Davis, and L. E. Scriven, Wetting hydrodynamics, Rev. Phys. Appl. **23**, 989 (1988).